Materials Today Communications 25 (2020) 101435

Contents lists available at ScienceDirect

Materials Today Communications

journal homepage: www.elsevier.com/locate/mtcomm

Characterizations of microstructure, crystallographic texture and mechanical properties of dissimilar friction stir welding joints for AA2024 and AA7075 under different tool shoulder end profiles

Chenghang Zhang[a,b,c], Guangjie Huang[a,b,*], Yu Cao[a,b], Qilei Li[a,b], Liqiang Niu[a,b], Qing Liu[d]

[a] International Joint Laboratory for Light Alloys (MOE), College of Materials Science and Engineering, Chongqing University, Chongqing 400044, PR China
[b] Shenyang National Laboratory for Materials Science, Chongqing University, Chongqing 400044, PR China
[c] Department of Materials Science and Engineering, KTH Royal Institute of Technology, SE-100 44, Stockholm, Sweden
[d] College of Materials Science and Engineering, Nanjing Tech University, Nanjing 211816, PR China

ARTICLE INFO

Keywords:
Aluminum alloys
Friction stir welding
Tool shoulder end profile
Microstructure
Texture
Mechanical properties

ABSTRACT

In this investigation, the influence of tool shoulder end profiles (concentric circle shoulder-CCS and three-helix shoulder-THS) and rotational speed (ROSP, 800, 1100, 1400 rpm) on microstructure and mechanical performance of the dissimilar FSW AA2024/7075 joints was analyzed in detail. The results indicated that the width of thermos-mechanical affected zone and the average grain size of nugget zone (NZ) in the CCS joints are lower than those in the THS joints, and they all increase with increasing the ROSP. There is a difference on the shear texture types generated in the different positions of the NZ in the CCS and THS joints. Tensile properties of the joints fabricated by employing the CCS tool are excellent compared to the THS tool. The maximum welding efficiency about 90.8 % can be obtained in the CCS joint at 1000 rpm. The fracture mode of the CCS and THS joints is ductile and brittle failure, respectively.

1. Introduction

At present, the joining of aluminum structural plates with reliable mechanical properties is required in the field of the aerospace and automotive applications [1,2]. High strength aluminum alloy (2xxx and 7xxx) plates are mainly used for structural components [3–5], the joining of 2xxx and 7xxx aluminum alloys is urgently needed [6]. Using conventional fusion welding methods to join these dissimilar aluminum alloys results in poor mechanical properties, due to their significant differences in physical, chemical and metallurgical properties [7]. Friction stir welding is an efficient solid-state joining technique [8,9], which has been successfully applied in the welding of dissimilar 2xxx/7xxx aluminum alloys [10], since it was invented by The Welding Institute (TWI) in 1991 [11]. Consequently, the FSW process is increasingly employed in the welding of a variety of metals and alloys [12].

Four stages occur in the FSW process [13–15], namely, (i) plunging, where the rotating tool including the shoulder and pin is inserted into the center line between the two plates till the shoulder contacts with the top surface of the plates; (ii) dwelling, where the material is softened to facilitate plastic deformation beneath the tool; (iii) traversing, where the tool moves along the welding center line to produce long butt welds; (iv) retracting, where the tool is retrieved after finishing the welding. The weld quality of the FSW joints mainly depends on the welding parameters [16–18] and the tool geometry [19]. Although the welding parameters play an important role in determining the heat input generated during FSW, the plastic deformation of material, such as friction, extrusion and shear behavior, is mainly controlled by the tool geometry [20–22]. The tool geometry is comprised of two parts: (i) the tool shoulder profile, transfers the heat generation from the FSW tool to the welded materials; (ii) the tool pin/probe profile, retains and mixes the plasticized/softened materials in the nugget zone (NZ) [23]. The tool shoulder (usually about three times of the plate thickness) generates more amount heat compared to the tool pin (usually about one third of shoulder diameter) [1,24]. They have a significant effect in peak temperature, material flow/mixing and mechanical behavior of the FSW aluminum alloy joints [25–27].

A few investigations have been performed to examine the influence of tool shoulder geometry on welding quality, material flow, microstructure and mechanical properties of the FSW joints. Leal et al. [28] adopted two types of tool shoulders (a conical cavity shoulder and a

* Corresponding author at: International Joint Laboratory for Light Alloys (MOE), College of Materials Science and Engineering, Chongqing University, Chongqing 400044, PR China.
E-mail address: gjhuang@cqu.edu.cn (G. Huang).

https://doi.org/10.1016/j.mtcomm.2020.101435
Received 29 April 2020; Received in revised form 4 July 2020; Accepted 5 July 2020
Available online 08 July 2020

scrolled shoulder) to study material flow behavior in dissimilar FSW AA5182-H111/6016-T4 joints. The results revealed that pin-driven flow was primary in the joint fabricated by the conical cavity shoulder, while the shoulder with scroll channel drags the plasticized material from edge towards the center and promotes the material mixing within the channels and around the pin. Mugada and Adepu [19,29,30] performed the researches about the shoulder end features and pin designs on axial force, temperature and mechanical properties of the FSW AA6082-T6 joints. They noticed that the joint fabricated with ridges shoulder tool leads to outstanding properties with prominently lower axial force (approximately 32 %). They also found that the hexagonal pin and pentagonal pin tools produce a reduced force behavior, while triangular pin designed tool facilitates an increasing force behavior in the process of welding. The triangular pin designed tool produces prominent mechanical properties of the joints. Trueba Jr. et al. [31] analyzed the impact of tool shoulder features on defects and tensile properties of the FSW AA6061-T6 joints and reported that high quality joints can be realized by using the shoulder with a raised spiral even if the welding conditions is non-ideal. Periyasamy et al. [32] made an attempt to analyze the effect of tool shoulder concave angle and pin profile on microstructure and mechanical performance of the FSW AA7075-T651/6061 joints and concluded that the maximum tensile strength (298 MPa), hardness (143 HV and bending angle (49°) can be achieved by employing 3° concave shoulder profile with square pin.

Several researchers analyzed the influence of shoulder diameter on material flow, thermal cycle and mechanical properties of the FSW joints. Shi et al. [21] worked on the influence of tool shoulder size on material flow and thermal process during FSW with ultrasonic vibration and observed that the maximum width of the shear region at the top surface of the joint has a direct relationship with the shoulder diameter. Padmanaban et al. [33] found that employing high shoulder diameter leads to low welding efficiency of the FSW joints. Zhang et al. [34] studied the temperature distributions and the materials deformation during FSW at different shoulder sizes by using a fully coupled thermo-mechanical model. They concluded that large shoulder diameter can result in the temperature rise and the enlarged stirring zone volume. Saravanan et al. [22] analyzed the microstructure and mechanical properties of the dissimilar FSW AA2024-T6/7075-T6 joints using five different shoulder diameter (D) to pin diameter (d) ratios (D/d ratio) and observed that the joint produced by employing D/d ratio of 3 displays better mechanical performance. Nathan et al. [35] investigated the influence of shoulder diameter to the sheet thickness ratio on mechanical properties of the FSW high strength low alloy (HSLA) steel joints. It is found that the joint with excellent mechanical properties can be acquired by employing the 25 mm of shoulder diameter (5 times the plate thickness).

Some authors have worked on the influence of tool pin geometry on material flow, microstructure and mechanical properties of the FSW joints. Kumar et al. [36] investigated the influence of tool pin profile (cylindrical thread-CT, plain cylindrical-PC, plain tapered cylindrical-PTC and square-SA) on the microstructure and particle distribution of friction stir processed Z60 magnesium surface composites. It is concluded that the surface composites produced by PTC pin profile exhibits excellent performances, which results from higher shear force and balanced state of material flow and heat generation. Raturi et al. [37] conducted the joint strength and failure research of dissimilar AA6061-T6/70750-T651 joints and concluded that good tensile strength and flexural load can be obtained by employing the cylindrical threaded with three flat faces and cylindrical grooved tool pin. Prakash et al. [38] explained the influence of four kinds of tool pin profiles on welded zone morphology of the joints. They observed that the stepped-conical pin profile produces high temperature and material flow velocity compared to all other tools. The stepped-conical pin profile tool results in the formation of the cylinder dominant vase shape, while all other tools lead to the formation of the basin dominant vase shape in the weld zone. Rao and Kumar [39] studied the pin geometry on the relationship between structure and property of dissimilar FSW AA6061/2014 joints. They found that high strength joints with defect-free can be acquired by adopting the polygonal hybrid square pin profiles.

In addition, Sun and Wu [40] investigated the influence of tool thread pitch on thermal process evolution in the FSW AA6061-T6 joints. They found that the speed sudden change at advancing side (AS) can be effectively prevented by using pin thread compared to unthreaded pin, and the total heat generation decreases with increasing thread pitch, which leads to low peak temperature during FSW. Ahmed et al. [41] investigated the influence of tool geometry on grain structure, texture and hardness of the FSW AA6082 joints (32 mm thickness), and reported that the tapered probe tool (TPT) leads to the variation of grain size and strain rate, while the parallel probe tool (PPT) produces far more uniform grain size and strain rate in the NZ. Compared to the PPT, the TPT produces a local shear reference frame with a tilt angle.

Although aforementioned considerable studies published in the literature have been conducted to address the utilization for high efficiency of tool shoulder features and pin geometries in the FSW joints, However, few studies about the influence of tool shoulder end profile on grain structure, crystallographic texture and mechanical properties of dissimilar FSW AA2024/7075 joints have been conducted. Therefore, the objective of this present investigation is to compare material flow, grain structure, crystallographic texture and mechanical properties of dissimilar FSW AA2024-T351/7075-T651 joints by using two kinds of tool shoulder end profiles.

2. Experimental methods

The as-received alloys AA2024-T351 and AA7075-T651 sheets (300 × 40 × 5 mm) were used as two base materials (BMs). Table 1 displays their nominal chemical compositions. The welding test was conducted on the FSW equipment (FSW-LM-AM16-2D), as exhibited in Fig. 1a. During FSW, the welding direction (WD) was perpendicular to the sheet rolling direction (RD) in the butt joint configuration. As stated in the previous literature [42,43], AA2024-T351 and AA7075-T651 sheets were put on the AS and retreating side (RS), respectively. Throughout the welding process, the welding speed and the tool tilting angles were kept as 120 mm/min and 2.5°, respectively. As shown in Fig. 1b, two different concave shoulder end profiles with concentric circle shoulder (CCS) and three-helix shoulder (THS) and different rotational speeds (ROSP, 800, 1100, 1400 rpm) were employed in this work. The shoulder diameter of the CCS tool was 15 mm, and the tip diameter of the tapered thread pin was 3.76 mm and 5 mm in length, while the shoulder diameter of the THS tool was 18 mm, as well as a tapered thread pin with 4.52 mm in tip diameter and 5 mm in length. The different joints are represented by the following different codes: CCS-800, CCS-1100, CCS-1400, THS-800, THS-1100, THS-1400, wherein, for example, the CCS-800 means that the joint was fabricated by using the CCS tool at 800 rpm.

The welded specimens were transversely cut by electric discharge machine perpendicular to the WD, then were carefully grinded and polished, thereafter etched with Keller reagent for 40 s to perform the optical microscopy (OM) and scanning electron microscopy (SEM, JEOL JSM-7800 F) tests. The electron backscatter diffraction (EBSD) measurement was carried out by using the field emission gun SEM (TESCAN MIRA3) equipped with a HKL-EBSD system. The measured step size was set to 0.3 μm.

Table 1
Chemical composition of the two BMs (in wt.%).

	Si	Fe	Cu	Mn	Mg	Cr	Zn	Ti	Al
2024-T351	0.05	0.17	4.5	0.6	1.4	0.01	0.03	0.02	Bal.
7075-T651	0.05	0.19	1.7	0.04	2.4	0.2	5.8	0.03	Bal.

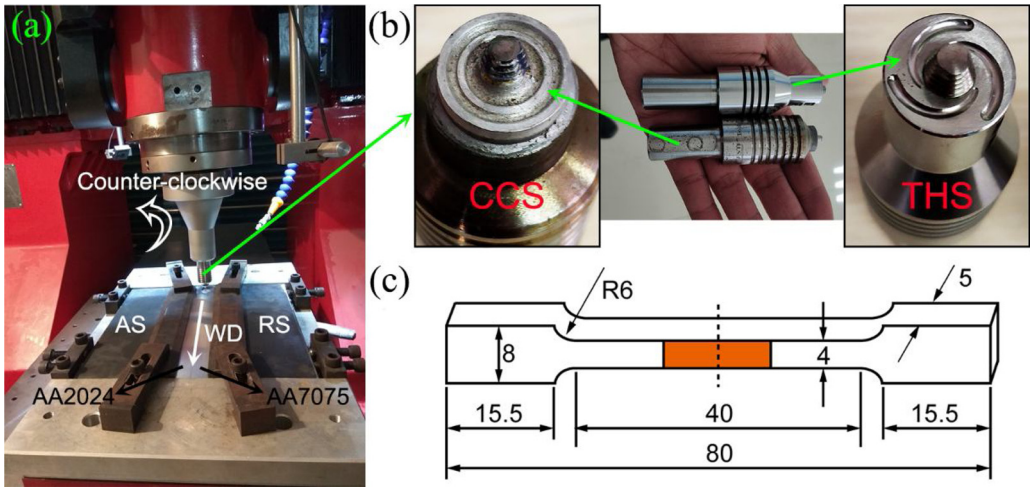

Fig. 1. The FSW process: (a) the FSW machine and the clamping platform, (b) the tools and (c) the size of the tensile samples.

Along the horizontal line at the center of the joint thickness, Vickers microhardness tests were conducted on the digital micro-hardness tester (MH-3) with a test load of 200 g and a dwell time of 10 s. The spacing between the neighbouring indentations was 1 mm. As exhibited in Fig. 1c, the flat dog-bone tensile samples were prepared, which were cut along the cross-section of the dissimilar joints. Tensile tests were carried out at a crosshead speed of 1 mm/min by using a Shimadzu AG-X plus universal testing machine. Three tested duplicates were intercepted from each dissimilar joint to guarantee the dependability of tensile result.

3. Results and discussion

3.1. Macrostructure of the dissimilar joints

Since the appearance of the joints can provide some useful information about the quality of the welds, surface defect usually is a visual manifestation of the internal defect of the joints, evaluating surface quality is a criterion for the joint quality. Furthermore, the exist hole was inspected as a function of the Lloyd's register (LR) [44]. The deformed material under the action of the tool always remains on the tool shoulder. 100 % complete around the circle hole can be considered as a good weld. The surface appearance and the cross-sectional macroscopic photographs of the dissimilar joints are displayed in Figs. 2 and 3, respectively. Obviously, it is noticed that all the joints form a complete circle around the hole (the green arrows in Fig. 2), and no defects, such as holes, can be found at the surface and the roots of the joints. As a result, we can consider that the ideal/non-defective dissimilar FSW joints can be obtained by using CCS and THS tools at three ROSPs. It can also be observed that material ripples are uniformly distributed at the surface of the joints, resulting from the processing combination of ROSP and welding speed. A little concavity (the yellow arrows in Fig. 2) is presented at the surface of all the joints, which is ascribed to the generation of a plunge depth when the tool is plugged into the top surface of the welded material. The formation of concavity can also reflect the fact that the tool shoulder hinders the plasticized/softened materials formed in the stir/weld zone from migrating outside, impelling them to flow towards around the pin [45]. Furthermore, the surface appearance of all the joints fabricated by CCS and THS tools is rough and fuzzy at low ROSP (Fig. 2a and d), and becomes brighter (Fig. 2c and f) with the increment of ROSP. This is because the degree of material mixing is limited at low ROSP, but more sufficient at higher ROSP. Besides, the width of the surface weld (Fig. 2) and cross-section (Fig. 3) of the NZ in the joints produced by CCS tool is smaller than that manufactured by THS tool. This is due to the fact that the shoulder diameter of the CCS is lower than that of the THS.

As exhibited in Fig. 3, first, the stir zone of all the six dissimilar joints is comprised of the dark and light zones, which corresponds to

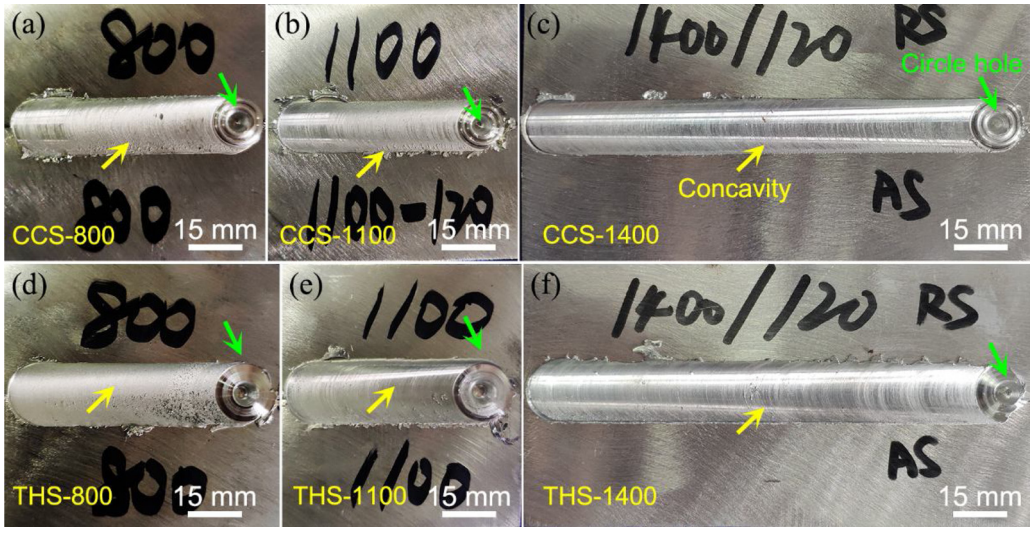

Fig. 2. Surface appearances of all the six joints.

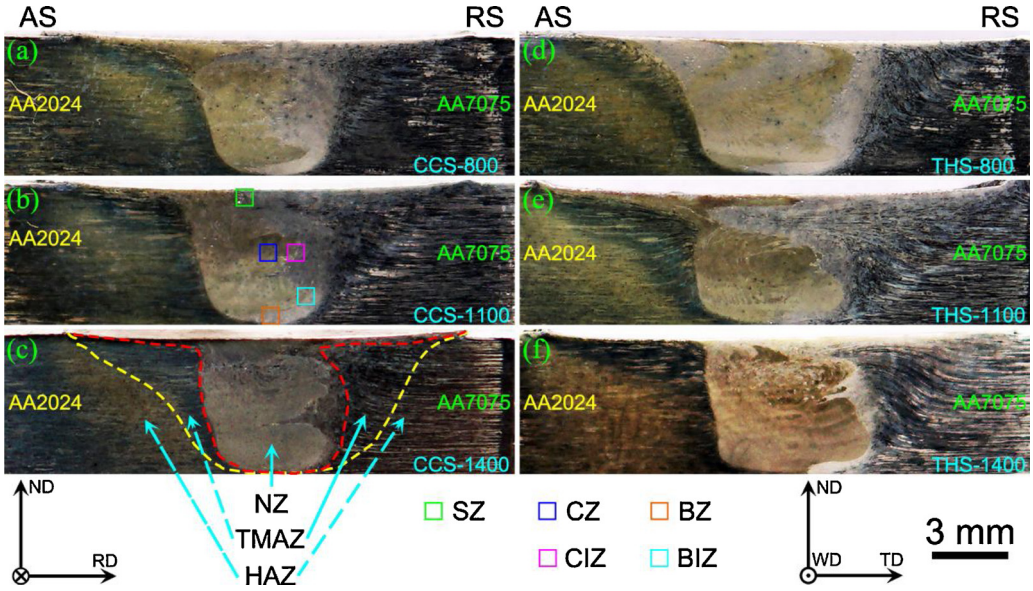

Fig. 3. Macroscopic appearances of in the six joint cross sections: (a) CCS-800, (b) CCS-1100, (c) CCS-1400, (d) THS-800, (e) THS-1100 and (f) THS-1400.

the AA2024 BM and AA7075 BM, respectively, as a result of their different degrees of chemical reactions to the Keller reagent. As a consequence, the flow behavior of materials can be obviously observed in the NZ. Second, the plasticized materials flow from the AS-A2024-T351 to the RS- AA7075-T651 under the action of the extrusion and stirring of the FSW tool. Third, the materials from the AS account for most of the stir zone compared to the RS. According to the cross section morphology of the dissimilar joint, five zones can be defined (Fig. 3c): the heat affected zone (HAZ) on the AS, the HAZ on the RS, the thermos-mechanical affected zone (TMAZ) on the AS (AS-TMAZ), the TMAZ on the RS (RS-TMAZ), the NZ. Meanwhile, on the basic of material flow characterization in the NZ, five zones can be further subdivided with different colors in Fig. 3: (i) shoulder zone (SZ), (ii) center zone (CZ), (iii) center interface zone (CIZ), (iv) bottom interface zone (BIZ) and (v) bottom zone (BZ).

3.2. Microstructure

In the field of FSW, the FSW joints of aluminum alloys are usually fractured in or near the TMAZ of the welded zone [13]. At present, the existing researches about the microstructure of the TMAZ in dissimilar FSW joints are not systematic and in-depth enough [46]. Accordingly, it is essential to study the microstructure evolution of the TMAZ in the joints. In this work, we quantitatively analyze the change in width of the TMAZ in the joints under different tool end profiles. Fig. 4 displays the SEM images of the AS-TMAZ and RS-TMAZ in all the dissimilar joints. It can be observed that different morphological characteristics can be found in the AS-TMAZ or RS-TMAZ in the dissimilar joints at different processing conditions. Through the measurement of the width of AS-TMAZ and RS-TMAZ, as exhibited in Fig. 5, the width of AS-TMAZ and RS-TMAZ in dissimilar joints fabricated by CCS or THS tool increases with the increment of ROSP. Ghosh et al. [47] proposed that the relationship between the peak temperature in the NZ (T_{NZ}) and the FSW processing parameters (ROSP (ω) and welding speed (v)) is shown below:

$$\frac{T_{NZ}}{T_m} = K\left(\frac{\omega^2}{v \times 10^4}\right)^{\alpha} \tag{1}$$

where the T_m is the melting point of metals, and the K and the α are the constant (wherein, the α is $0.04-0.06$ and the K is $0.65-0.75$). It can be concluded that the T_{NZ} increases with increasing the ROSP, meaning high heat input in the NZ at high ROSP, leading to widened AS-TMAZ and RS-TMAZ in the dissimilar joints. In addition, it can be also found that the width of AS-TMAZ and RS-TMAZ of the joints produced by CCS tool is smaller than those the joints fabricated by THS tool in the conditions of the same ROSP. This can be ascribed to the higher heat input produced in the joints fabricated by THS tool, leading to high width of the AS-TMAZ and RS-TMAZ. This phenomenon has also been verified by Liu et al. [48].

During FSW, the deformation mechanism can be determined by the strain rate and temperature resting with the grain morphology. Hassan et al. [49] and Gholinia et al. [50] reported that the strain exacted for starting the dynamic recrystallization (DRX) can be defined as follow:

$$\varepsilon_{crit} = \ln(Z^{\frac{1}{m}}d_0) + C \tag{2}$$

in which Z is the Zener-Hollomon parameter, as shown in Eq. (3) d_0 is the initial grain width, m and C are the constants.

$$Z = \dot{\varepsilon} exp\left(\frac{Q}{RT}\right) \tag{3}$$

in which $\dot{\varepsilon}$ is the strain rate, Q, R and T are the action energy, universal gas constant and deformation temperature, respectively. According to the Eqs. (3–4), we can understand that the ε_{crit} for the activation of DRX decreases with the increment of temperature, and with the decrease of strain rate and grain size. Fig. 6 is the OM images of the grains in the CZ of the dissimilar joints. It can be seen that bulk fine grains are produced in the CZ of all the dissimilar joints. This can be due to the occurrence of DRX resulting from the severe plastic deformation and high heat input during FSW. Besides, we can find that the grain size in the CZ of all the dissimilar joints increases with the increment of ROSP. On the basic of the Eq. (1), with the increment of ROSP, high peak temperature in the NZ (T_{NZ}) can be produced at high ROSP, meaning that high heat input can be generated at high ROSP, which induces the grain growth. Through comparative study, overall speaking, the grain size in the CZ of the joints fabricated by CCS tool is lower than that produced by THS tool at the same EOSP. This is because the THS tool can produce higher heat input compared to the CCS tool, leading to large grain size presenting in the CZ of the joints fabricated by the THS tool. This is consistent with the variation trend of the width of the above TMAZ. In order to detailedly analyze the difference of the grain size in the dissimilar joints produced by the CCS and THS tools, we conduct the EBSD measurement on the different positions in the NZ (SZ, CZ, BZ, CIZ and BIZ, as marked in Fig. 3) of the dissimilar joints at the ROSP of 1400 rpm.

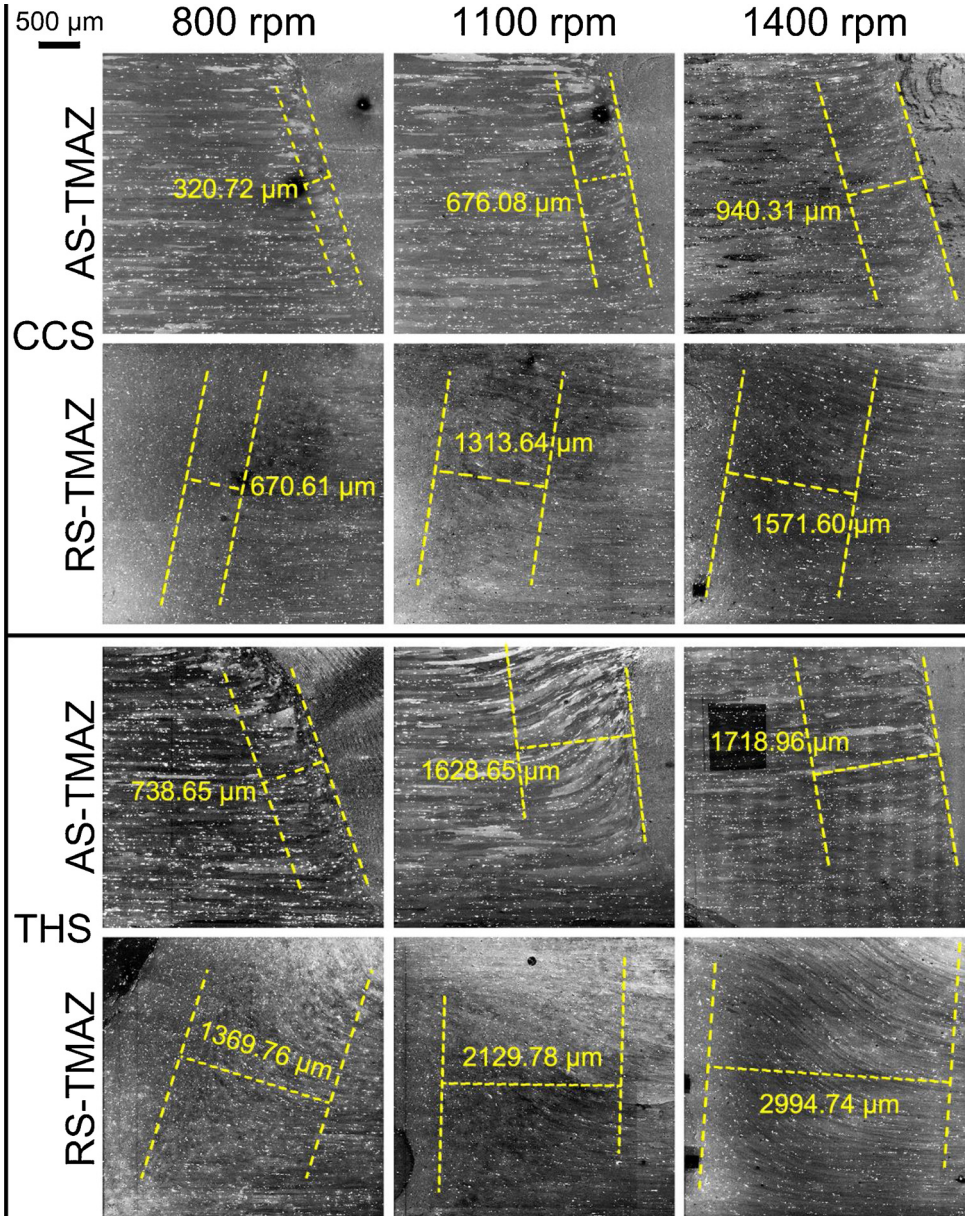

Fig. 4. The SEM images of AS-TMAZ and RS-TMAZ in the six dissimilar joints.

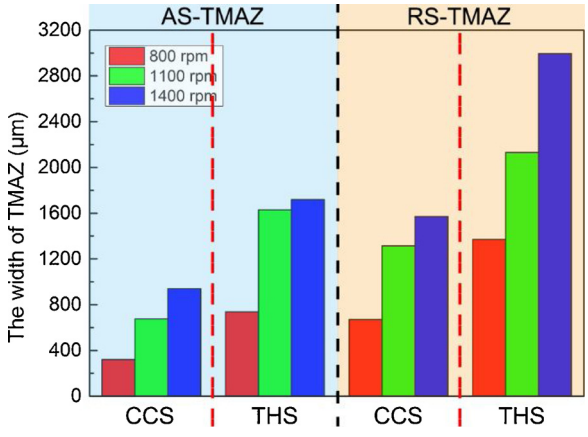

Fig. 5. The statistics of the width of the AS-TMAZ and RS-TMAZ in the six dissimilar joints.

The EBSD measurements about the grain characteristics in the SZ, CZ, BZ, CIZ and BIZ are displayed in Figs. 7 and 8, these images are the band contrasts (BC) and the corresponding orientation distribution maps, which were acquired by Channel 5 software. In the BC and orientation distribution maps (Figs. 7 and 8), the grain boundaries are composed of the low angle grain boundaries (LAGBs) from 2° to 15° marked with the white lines and the high angle grain boundaries (HAGBs) over 15° labelled by employing the black lines. Fig. 9a–e show the gran size distribution of the above five local zones in the dissimilar joints fabricated by CCS and THS tools and Fig. 9f exhibits the statistics of the average grain size of the above five zones. Fig. 10a–e display the misorientation angle distribution of the local zones in the dissimilar joints fabricated by CCS and THS tools and Fig. 10f demonstrates the statistics of the number fraction of LAGBs and HAGBs in the above five zones in the NZ of the two joints.

As displayed in Figs. 7 and 8, apparently, a large number of equiaxed grains with small size are formed in all the five local regions (SZ, CZ, BZ, CIZ and BIZ) of the six dissimilar joints. In theory, due to high stacking fault energy (SFE), the aluminum alloys may experience

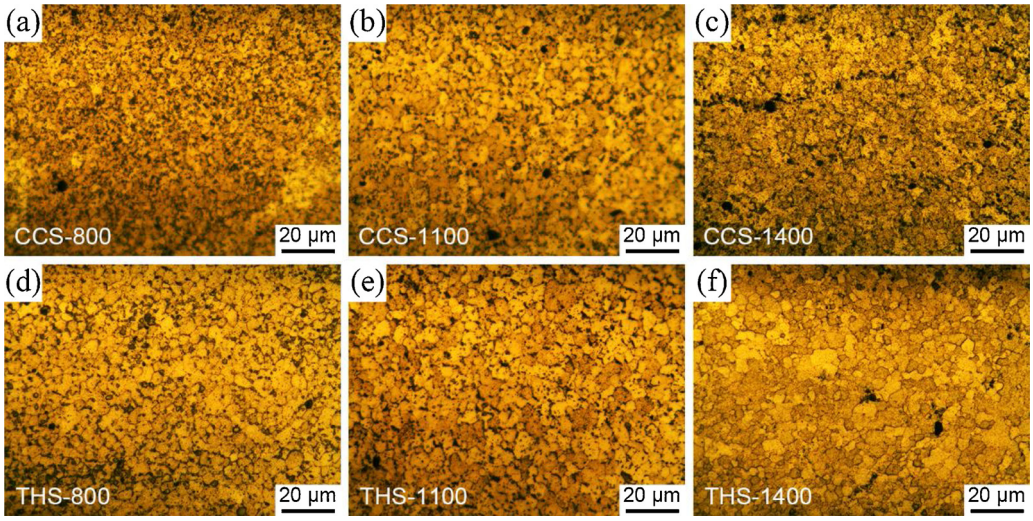

Fig. 6. The OM images of the CZ in the six dissimilar joints: (a) CCS-800, (b) CCS-1100, (c) CCS-1400, (d) THS-800, (e) THS-1100 and (f) THS-1400.

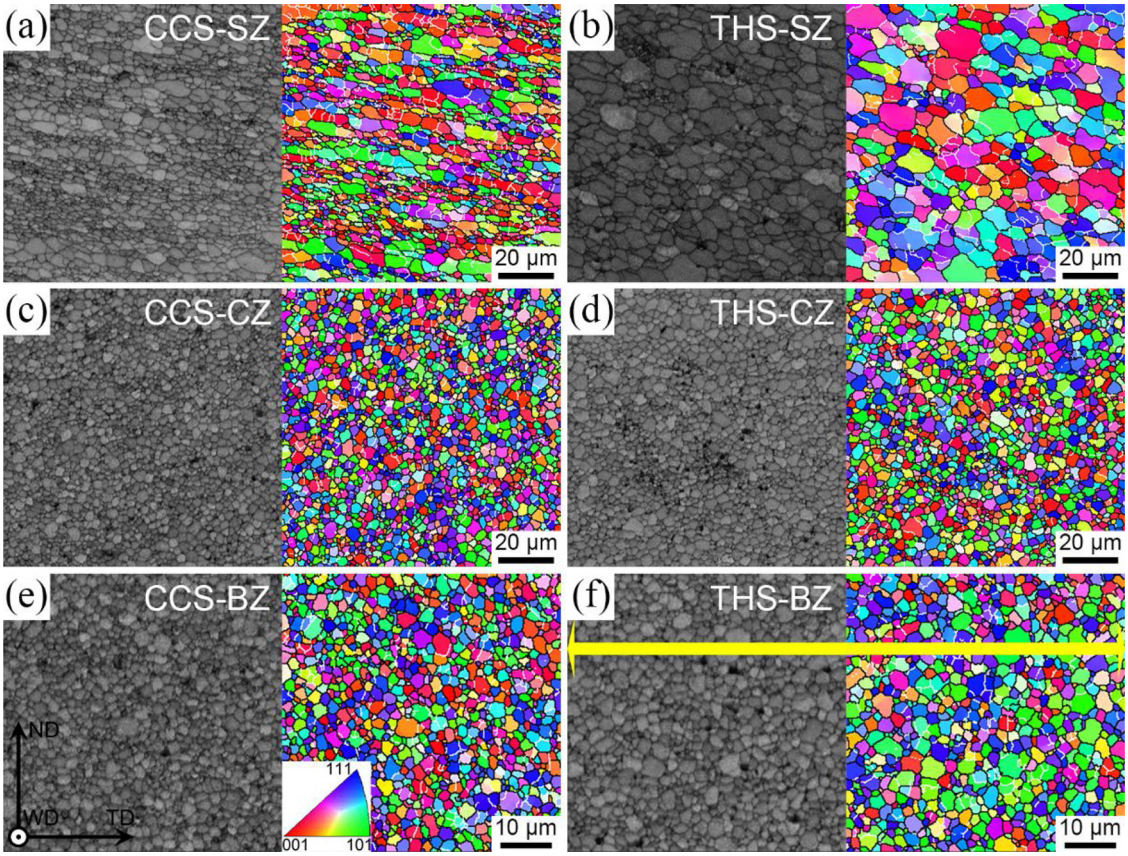

Fig. 7. The BC and orientation distribution maps in the NZ: (a) CCS-SZ, (b) THS-SZ, (c) CCS-CZ, (d) THS-CZ, (e) CCS-BZ and (f) THS-BZ.

continuous dynamic recrystallization-CDRX, discontinuous dynamic recrystallization-DDRX and geometric dynamic recrystallization-GDRX in the process of hot deformation [13,51]. The violent plastic deformation and the associated with high peak temperature facilitate the dynamic recrystallization, which leads to the formation of the recrystallized grains with HAGBs and grain refinement in the NZ.

As demonstrated in Figs. 7–10, the average grain size and the number fraction of the LAGBs in the SZ are higher than those in other four zones (CZ, BZ, CIZ and BIZ). This can be ascribed to the fact that the original grains in the SZ undergo violent distortion deformation under the extrusion action of tool shoulder and a large number of broken grains remain in the SZ. These characteristics usually occur near the tool shoulder by reason of high strain and sharp thermal gradient from the tool shoulder to the surface of the welded materials, resulting in the formation of dense sub-grain boundaries [52,53]. On the other hand, Figs. 9 and 10 indicated that the average grain size increases and the number fraction of LAGBs decreases from the CZ (CIZ) to the BZ (BIZ). This microstructure difference can be ascribed to the differences in the peak temperature, strain rate and cooling rate in the CZ (CIZ) and the BZ (BIZ) of the dissimilar joints.

Interestingly, through the statistics of the number of the grains with small size (Fig. 8c and d, $\leq 2\,\mu m$) in the BIZ after removing the grains

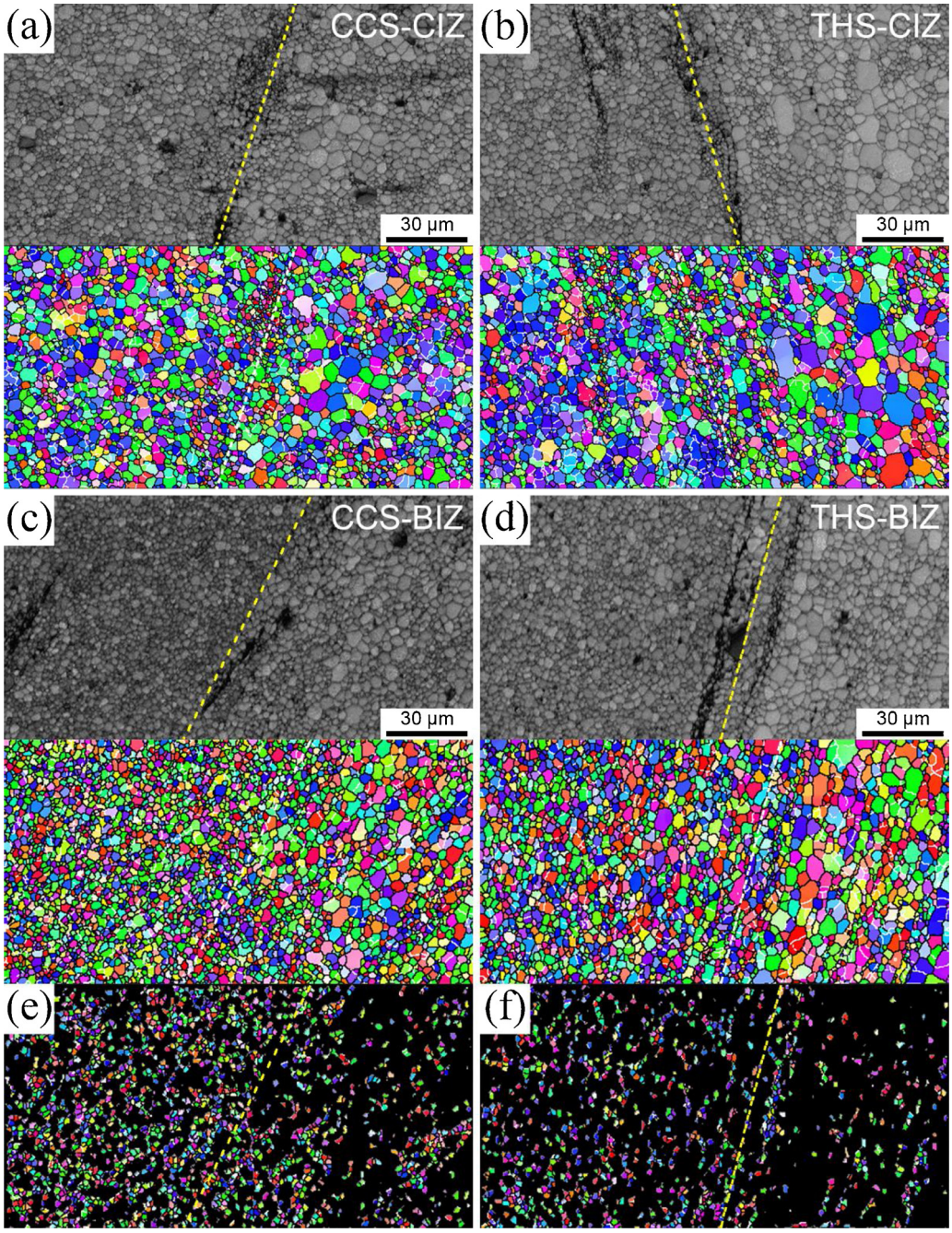

Fig. 8. The BC and orientation distribution maps in the NZ of the dissimilar joints: (a) CCS-CIZ, (b) THS-CIZ, (c) CCS-BIZ, (d) THS-BIZ, the small grains distribution after removing large grains (> 2 μm): (e) CCS-BIZ and (f) THS-BIZ.

with large size (> 2 μm), it is found that the number of the grains with small size in the BIZ of the joint fabricated by CCS tool is more than that produced by THS tool. Furthermore, we can clearly observe from Figs. 7–9 that the average grain size of the SZ, CZ, BZ, CIZ and BIZ in the NZ of the joint manufactured by CCS tool is low compared to the joint produced by THS tool. These above results are mainly related to the grain growth caused by different heat inputs generated by using two kinds of the shoulder tools: CCS and THS. The grain growth takes place mainly through curvature reduction of grain boundaries and geometric conflation of grains [54,55]. It can be seen from Figs. 7 and 8 that some LAGBs are situated at the grain boundaries or the grain interior with large size, their formation results from the dynamic recovery (DRV) mechanism and the static recovery after the DRV in the process of cooling cycle [56]. Since these LAGBs posses the similar orientations, creating powerful conditions for grain consolidation to occur more easily. Thus, two or more grains can be combined together to form a larger grain under the action of thermal cycling generated during FSW [57]. The THS tool produces more heat input/thermal cycle than the CCS tool, which gives rise to the generation of larger grains until the following phenomena appear [58]: (i) the particles pinning the grain boundaries, (ii) the development of stable crystallographic orientations and (iii) the marked decrease in temperature. Accordingly, the number of the grains with small size in the BIZ of the joint produced by THS tool is low compared to the CCS tool, while the average grain size in the joint manufactured by the THS tool is high compared to the CCS tool. In addition, by comparing the average grain size on the different positions in the same joint, we can conclude that the grain structure of the joint produced by the CCS tool is more uniform than that fabricated by the

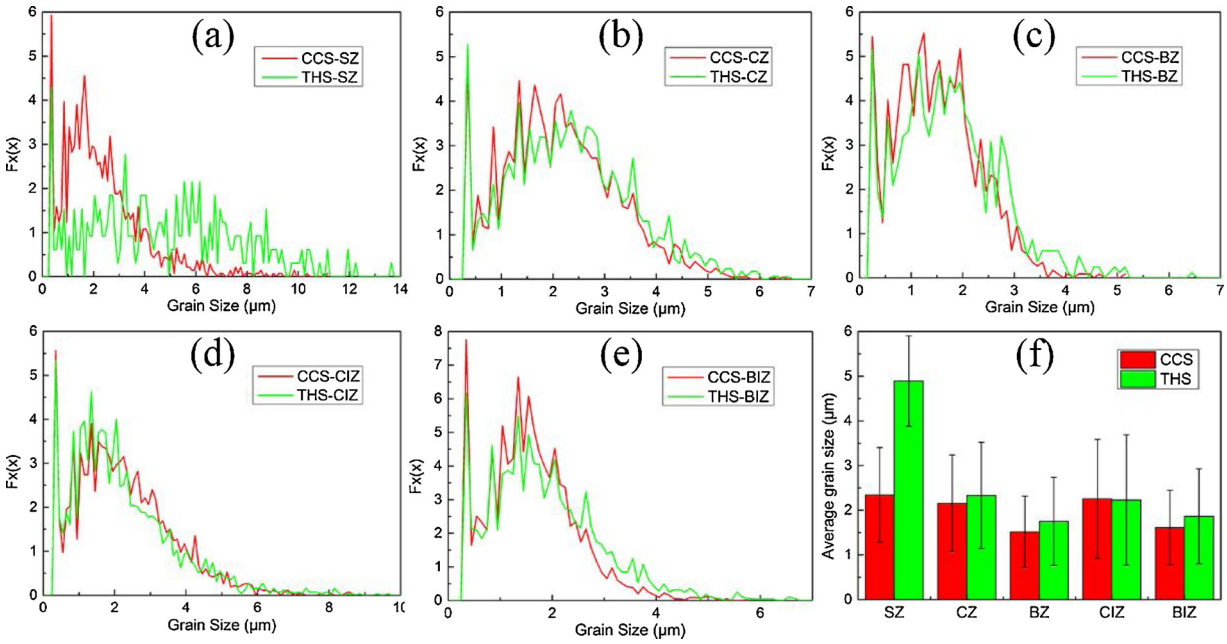

Fig. 9. Gran size distribution of the local zones in the dissimilar joints fabricated by CCS and THS tools (a) SZ, (b) CZ, (c) BZ, (d) CIZ, (e) BIZ and the statistics of the average grain size of the above five zones (f).

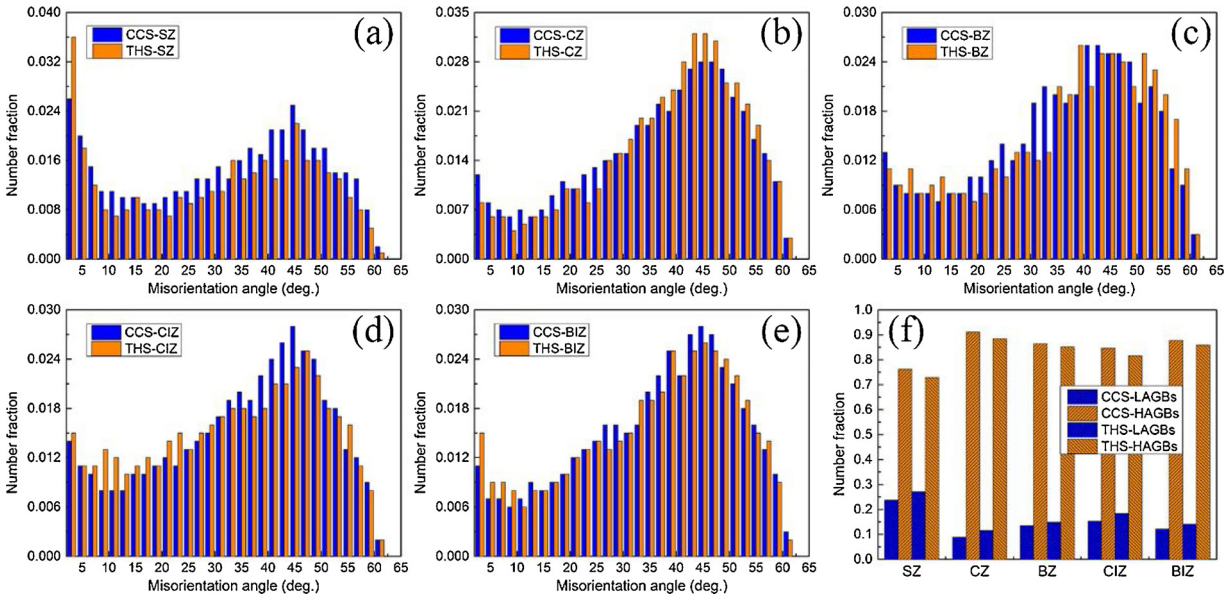

Fig. 10. Misorientation angle distribution of the local zones in the dissimilar joints fabricated by CCS and THS tools (a) SZ, (b) CZ, (c) BZ, (d) CIZ, (e) BIZ and the statistics of the number fraction of grain boundaries in the above five zones (f).

THS tool. This can result from the fact that the heat input generated by the CCS tool is more evenly distributed than the THS tool.

Many studies mainly focus on the effect of tool geometry on morphology, grain structure and temperature distribution of the welded zone in the FSW joints [22,29,30,59,60], the influence of tool geometry on texture formation in the NZ has been rarely reported. Ahmed et al. [41] investigated the effect of tool geometry in crystallographic Texture the FSW AA6082 joints, However, the texture types in the different positions of the NZ of the joints under different tool end profiles are still unclear. During FSW, although material flow behavior is complex, the primary deformation mode is regarded as shear deformation. In general, the shear textures are represented by crystallographic plane $\{hkl\}$ and crystallographic direction $\langle uvw\rangle$, which is identified with the shear plane and shear direction, respectively. Regarding to the fcc metals, $\{hkl\}\langle 110\rangle$ and $\{111\}\langle uvw\rangle$ fibers are the main texture types [61]. SFE has a significant effect on the texture formation for aluminum alloys, thus, we analyzed the crystallographic texture by adopting 111 pole figure (PF) and orientation distribution function (ODF, $\varphi_2 = 0^o$ and 45^o) in the NZ including SZ, CZ, BZ, CIZ and BIZ of the dissimilar joints fabricated by CCS and THS tools at 1400 rpm, as exhibited in Fig. 11.

As demonstrated in Fig. 11a and b, the SZ in the CCS joint contains $\{1\bar{1}1\}\langle 110\rangle$ A, $\{\bar{1}1\bar{1}\}\langle\bar{1}\bar{1}0\rangle$ $\overline{A}$, $\{1\bar{1}2\}\langle 110\rangle$ B, $\{\bar{1}1\bar{2}\}\langle\bar{1}\bar{1}0\rangle$ $\overline{B}$ and bits of $\{001\}\langle 110\rangle$ C components, while the SZ in the THS joint consists of $\{111\}\langle\bar{1}\bar{1}2\rangle$ A_1^*, $\{111\}\langle 11\bar{2}\rangle$ A_2^* and $\{001\}\langle 110\rangle$ C components. As shown in Fig. 11c and d, $\{001\}\langle 110\rangle$ C, bits of $\{1\bar{1}2\}\langle 110\rangle$ B and $\{\bar{1}1\bar{2}\}\langle\bar{1}\bar{1}0\rangle$ $\overline{B}$ can be observed in the CZ of the CCS joint, while $\{111\}\langle\bar{1}\bar{1}2\rangle$ A_1^*, $\{111\}\langle 11\bar{2}\rangle$ A_2^*, $\{1\bar{1}1\}\langle 110\rangle$ A and $\{\bar{1}1\bar{1}\}\langle\bar{1}\bar{1}0\rangle$ $\overline{A}$ can be noted as major texture components in the CZ of the THS joint. For the texture development in the BZ,

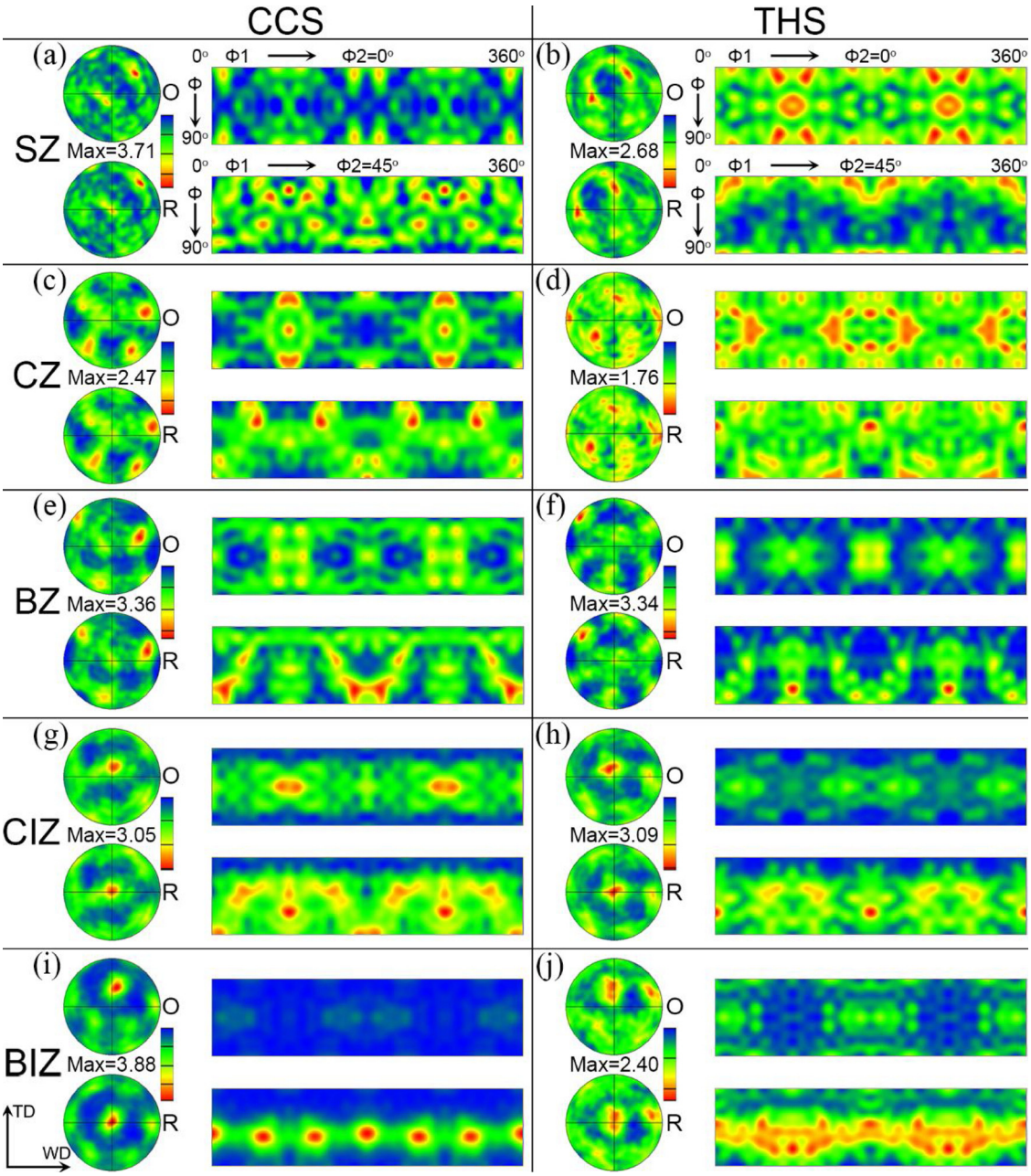

Fig. 11. 111 PF and ODF ($\varphi_2 = 0^o$ and 45^o) of the local zones in the dissimilar joints fabricated by CCS and THS tools.

we can find that $\{001\}\langle 110\rangle$ C, a lesser extent of $\{1\bar{1}2\}\langle 110\rangle$ B and $\{\bar{1}1\bar{2}\}\langle\bar{1}\bar{1}0\rangle$ $\bar{B}$ are presented in the BZ of the CCS and THS joints (Fig. 11e and f). For the texture analysis of the interface zone (Fig. 11g–j), $\{001\}\langle 110\rangle$ C, slight $\{1\bar{1}2\}\langle 110\rangle$ B and $\{\bar{1}1\bar{2}\}\langle\bar{1}\bar{1}0\rangle$ $\bar{B}$ are presented in the CIZ of the CCS joints (Fig. 11g), while $\{111\}\langle\bar{1}\bar{1}2\rangle$ A_1^*, $\{111\}\langle 11\bar{2}\rangle$ A_2^*, $\{1\bar{1}2\}\langle 110\rangle$ B and $\{\bar{1}1\bar{2}\}\langle\bar{1}\bar{1}0\rangle$ $\bar{B}$ are developed in the CIZ of the THS joints (Fig. 11 h). In addition, $\{1\bar{1}2\}\langle 110\rangle$ B and $\{\bar{1}1\bar{2}\}\langle\bar{1}\bar{1}0\rangle$ $\bar{B}$ can be found and formed in the BIZ of the CCS and THS joints as dominating texture components (Fig. 11i and j). Through comparison of the texture components in the CCS and THs joints, $\{111\}\langle\bar{1}\bar{1}2\rangle$ A_1^* and $\{111\}\langle 11\bar{2}\rangle$ A_2^* are mainly generated in the NZ excluding the BZ of the THS joints. According to the reports from Shen et al. [62] that the shear texture types are closely related to the shear strain magnitude, $\{111\}\langle\bar{1}\bar{1}2\rangle$ A_1^* and $\{111\}\langle 11\bar{2}\rangle$ A_2^* can be principally formed under the condition of low strain compared to other shear texture components. Consequently, it can be concluded that low strain is presented in the NZ of the THS joint compared with the CCS joint. Whereas, due to the $\{1\bar{1}2\}\langle 110\rangle$ B and $\{\bar{1}1\bar{2}\}\langle\bar{1}\bar{1}0\rangle$ $\bar{B}$ components forming in the SZ and CZ of the CCS joint, high strain is produced in the SZ and CZ of the CCS joint compared to the THS joint. The CCS and THS tools produce the same shear texture components in the BZ and BIZ, which indicates that the same magnitude of shear strain are formed in the BZ and BIZ whether by using the CCS tool or the THS tool.

3.3. Mechanical properties

Fig. 12 portrays the microhardness profiles of the six dissimilar joints. Obviously, the microhardness distribution of all the six dissimilar joints is characterized by the typical W-shape. Compared to the two BMs, the low microhardness zone is presented in the stir zone of all the dissimilar joints. This hardness softening phenomenon is primarily attributed to the occurrence of coarsening and dissolution of precipitated phases for solution strengthening aluminum alloys, resulting from high heat input/thermal cycle and violent plastic deformation produced

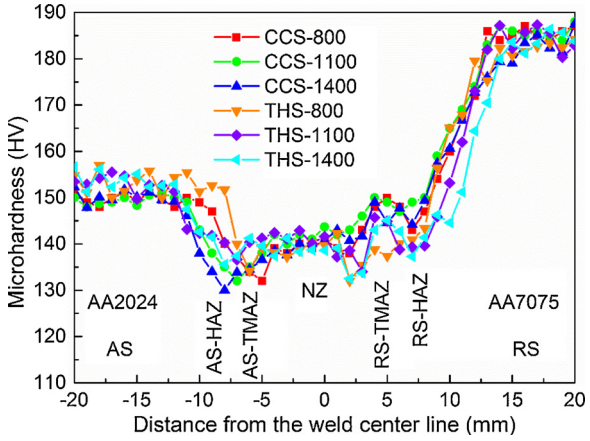

Fig. 12. Microhardness distribution of the six dissimilar joints.

during FSW [13]. The width of the low microhardness zone in the NZ of all the CCS joints is lower than that of all the THS joints. This is due to the case that the shoulder diameter of the CCS tool is lower than that of the THS tool. Furthermore, we find that the minimum microhardness value with 130 HV exists in the AS-HAZ of the CCS-1400 joint for the CCS joints. Nevertheless, for the THS joints, the minimum microhardness value with 132.5 HV can be found in the NZ on the RS (RS-NZ) of the THS-1400 joint. It can be concluded that the minimum microhardness of both the CCS and THS joints appears at higher ROSP (1400 rpm). This is because high ROSP produces more heat input. As a result, the precipitated phase is more prone to be dissolved and coarsened during FSW [51], leading to the decrease of microhardness.

Fig. 13a demonstrates the tensile curves of all the six dissimilar joints and the corresponding tensile data are summarized in Table 2. It is found from Fig. 13a and Table 2 that the yield strength (YS), ultimate tensile strength (UTS) and tensile elongation (TE) of all the dissimilar joints are inferior to those of the two BMs (AA2024 and AA7075). Regarding to the solution strengthening aluminum alloys, since FSW is approximately equivalent to a hot processing process, causing a large number of precipitates to coarsen, dissolve and re-precipitate after subsequent cooling [51], resulting in significant deterioration of the mechanical properties of the FSW joints compared to the corresponding BMs. It can be concluded that the YS and UTS of the CCS and THS joints increase first and then decrease with the increase of ROSP, which is similar to our previous research [7,10]. In addition, the maximum YS, UTS and TE can be acquired in the CCS-1100 joint, and which are 316.2 MPa, 426.8 MPa and 8.32 %, respectively. However, the minimum value including YS, UTS and TE can be obtained in the THS-1400 joint, which are 282.4 MPa, 386.6 MPa and 2.49 %, respectively. Compared to the THS joints, the YS, UTS and TE of the CCS joints are

Table 2
Summary of Tensile test results of the BMs and the dissimilar FSW joints.

Materials	YS/MPa	UTS/MPa	TE/%	Fraction locations	Efficiency
2024 BM	360	470	20.3	–	–
7075 BM	476	555	11.4	–	–
CCS-800	304.1	421.1	6.85	AS-TMAZ	89.6 %
CCS-1100	316.2	426.8	8.32	AS-HAZ	90.8 %
CCS-1400	293.8	419.3	8.52	AS-HAZ	89.2 %
THS-800	287.3	387.8	3.51	RS-NZ	82.5 %
THS-1100	298.6	411.9	5.05	RS-NZ	87.6 %
THS-1400	282.4	386.6	2.49	RS-NZ	82.3 %

higher than those of the THS joints under the same ROSP. When applying a load, fine grains produced by the CCS tool (Figs. 6–8) can impede dislocations, reducing the accumulation of dislocations during stretching. Meanwhile, the precipitated particles with more dispersed distribution could obstruct the movement of dislocations, thereby reducing the stress concentration and crack initiation [63]. Although some micro-cracks are generated, higher propagation resistance can ameliorate the mechanical properties [23]. However, the THS tool produces high heat input in comparison to the CCS tool, which gives rise to coarsening of grains and precipitated particles in the NZ of the joints, causing serious stress concentration, which is more likely to form cracks and lower the tensile performances of the joints [63]. The joint welding efficiency can be expressed by using the following equation:

$$\%\,Joint\ welding\ efficiency = \frac{UTS_{The\ welded\ joint}}{UTS_{AA2024\ BM}} \quad (4)$$

on the grounds of the Eq. (4), the maximum welding efficiency with 90.8 % can be obtained in the CCS-1100 joint.

The fracture places of all the six dissimilar joints are shown in Fig. 13b and outlined in Table 2. Clearly, the CCS-800 joint is fractured in the AS-TMAZ, and with increasing the ROSP, the fractures of the CCS-1100 and CCS-1400 joints are located in the AS-HAZ. High heat input is produced at high ROSP and the temperature on the AS is high compared to the RS [63], which results in the occurrence of precipitated phase particles coarsening in the AS-HAZ. For the THS joints, the fracture places of all the three dissimilar joints are located in the RS-NZ, indicating that the RS-NZ is the weak part for the THS tool. We can find that the fracture positions of all the dissimilar joints are consistent with the corresponding minimum microhardness value in Fig. 12. As is known to us, the UTS of the precipitation-reinforced aluminum alloys FSW joints with no defects is chiefly influenced by the precipitation phase characteristics and dislocation density. The influence of precipitate phases on mechanical properties can also be verified by their impact on the distribution of microhardness values. Thus, the tensile properties largely rely on the microhardness distribution of the FSW joints [60]. The lower microhardness means the lower UTS [64].

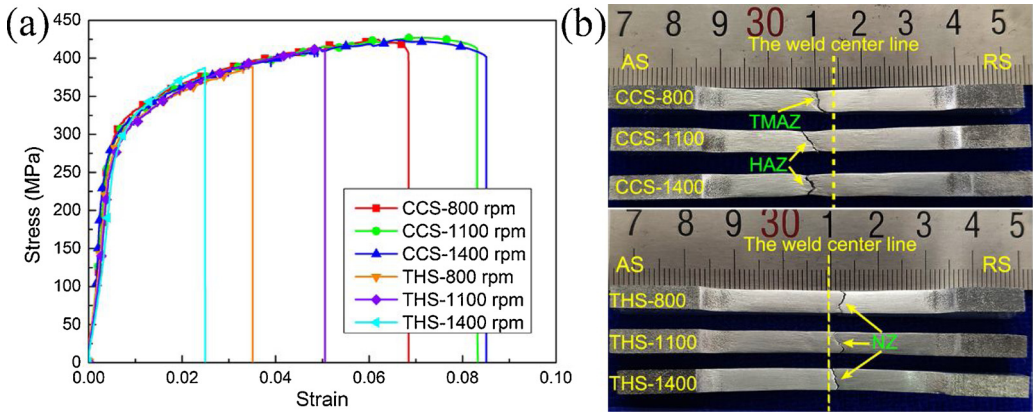

Fig. 13. Tensile measurements (a) tensile curves and (b) fracture location of the six dissimilar joints.

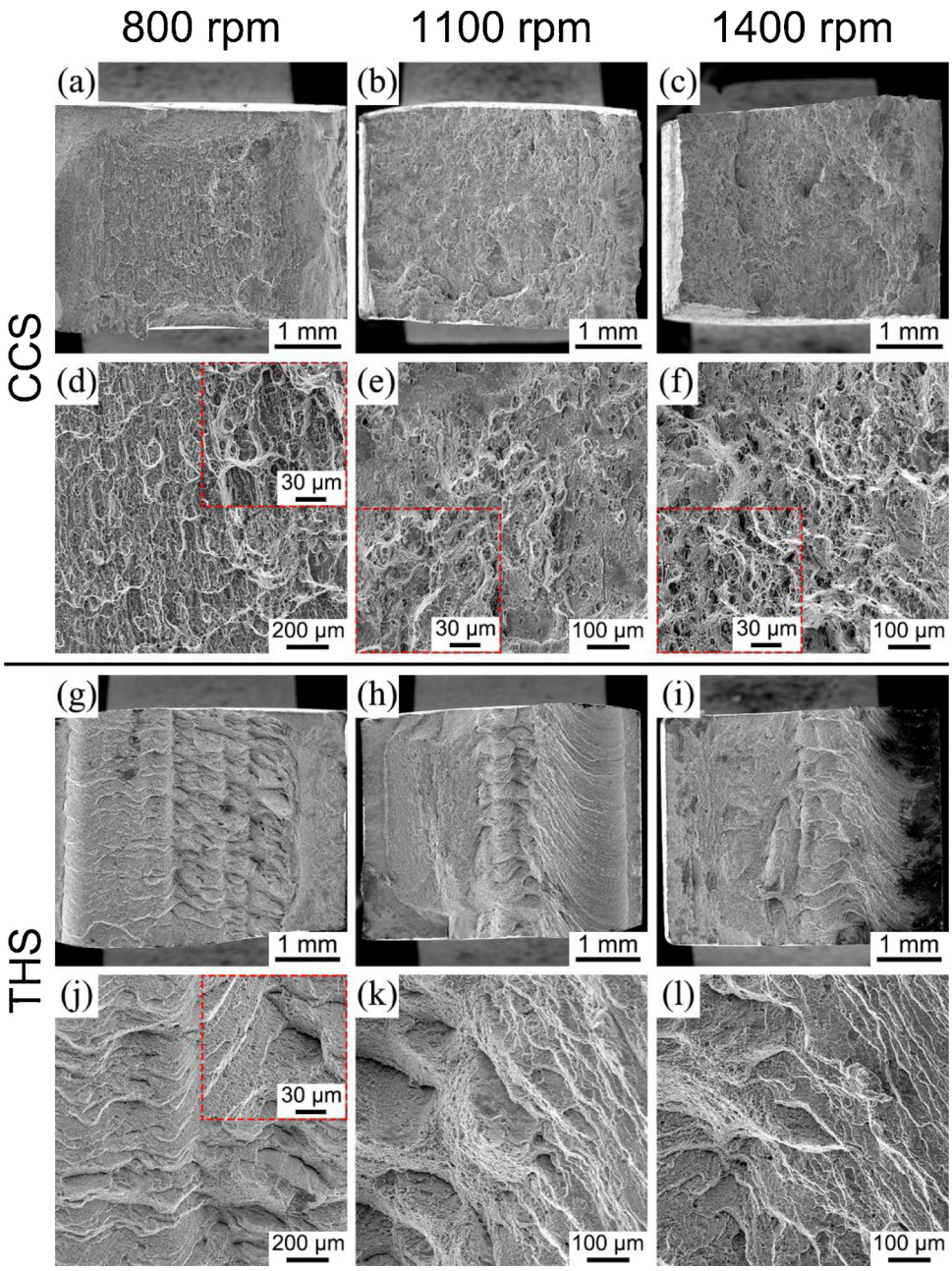

Fig. 14. Tensile fracture features of the dissimilar joints: (a and d) CCS-800, (b and e) CCS-1100, (c and f) CCS-1400, (g and j) THS-800, (h and k) THS-1100 and (I and l) THS-1400.

Fig. 14 displays the fracture surface features of the joints after conducting the tensile test. It can be noted that the fracture of all the joints initiates along the trajectory of material flow. As displayed in Fig. 14a–f, the fracture surface of all the CCS joints is characterized by the large tearing ridges as well as abundant deep dimples with large and small sizes, which reveals ductile fracture mode. However, it can be observed from Fig. 14g–l that many shallow dimples with small size are presented on the fracture surface of all the THS joints. Besides, it can be also observed that substantial cleavage steps are produced. Thus, the fracture mode of the THS joints is brittle failure. During crack propagation, the cleavage steps between the parallel cleavage planes with different heights, forming a river pattern and the flow direction of the river is in accordance with the crack propagation direction. Since the cleavage plane is a specific low exponential crystal plane, brittle fracture takes place along the cleavage plane. According to our previous work [65], the coarsening Fe-rich and Fe-Mn-rich constituent particles are formed in the TMAZ of the dissimilar FSW AA2024/7075 joints. These hardness brittle phases distributed in the form of chains results in a significant decrease of the ability of local plastic deformation, which weakens material's resistance to fracture propagation and makes it easier to expand, thus showing a brittle fracture behavior [66].

4. Conclusions

In this research, the influence of tool shoulder end profiles and ROSP on the microstructure and mechanical properties of the dissimilar FSW AA2024/7075 joints was studied. Some conclusions can be described as follows.

(1) Defect-free dissimilar FSW AA2024/7075 joints with were successfully fabricated by adopting the CCS and THS tools.
(2) The width of the TMAZ (AS-TMAZ and RS-TMAZ) in the CCS joints

is lower than that in the THS joints, and both of them increase with the increment of ROSP.

(3) The average grain size in the NZ of the CCS and THS joints increases with the enhancement of the ROSP. The average grain size in the NZ including SZ, CZ, BZ, CIZ and BIZ of the CCS joints is low compared to the THS joints.

(4) Same shear texture components are generated in the BZ ($\{001\}\langle 110\rangle$ C, slight $\{1\bar{1}2\}\langle 110\rangle$ B and $\{\bar{1}1\bar{2}\}\langle\bar{1}\bar{1}0\rangle$ $\bar{B}$) and BIZ ($\{1\bar{1}2\}\langle 110\rangle$ B and $\{\bar{1}1\bar{2}\}\langle\bar{1}\bar{1}0\rangle$ $\bar{B}$). However, compared to the CCS joint, $\{111\}\langle\bar{1}\bar{1}2\rangle$ A_1^* and $\{111\}\langle 11\bar{2}\rangle$ A_2^* components are only generated in the NZ excluding BZ of the THS joint.

(5) ROSP has an obvious influence on the tensile properties on the joints. The YS and UTS of the CCS and THS joints increase first and then decrease with the increase of ROSP. The tensile properties of the CCS joints are better than those of the THS joints. The maximum YS, UTS and TE can be acquired in the CCS-1100 joint, and which are 316.2 MPa, 426.8 MPa and 8.32 %, respectively. The corresponding maximum welding efficiency is approximately 90.8 % of AA2024 BM.

(6) The fracture of the dissimilar joints is located in the minimum microhardness value region. The fracture mode of the CCS joints is ductile failure, while the THS joints exhibit brittle fracture mode.

Data availability statement

The raw/processed data required to reproduce these findings cannot be shared at this time due to technical or time limitations.

The datasets generated during and/or analysed during the current study are available from the corresponding author on reasonable request.

Declaration of Competing Interest

The authors declare that there are no conflicts of interest.

Acknowledgements

The “National Natural Science Foundation of China” (No. 51421001) and “Fundamental Research Funds for the Central Universities” (No. 2018CDJDCL0019 and No. 2020CDJQY-A003) are greatly acknowledged for financial support. Authors also greatly acknowledge the Electron Microscopy Center of Chongqing University for providing SEM and TEM test channel.

References

[1] G. Padhy, C. Wu, S. Gao, Friction stir based welding and processing technologies-processes, parameters, microstructures and applications: a review, J. Mater. Sci. Technol. 34 (2018) 1–38.
[2] O. Kayode, E.T. Akinlabi, An overview on joining of aluminium and magnesium alloys using friction stir welding (FSW) for automotive lightweight applications, Mater. Res. Express 6 (2019) 112005.
[3] T. Dursun, C. Soutis, Recent developments in advanced aircraft aluminium alloys, Mater. Des. 56 (2014) 862–871.
[4] X. Zhang, Y. Chen, J. Hu, Recent advances in the development of aerospace materials, Prog. Aerosp. Sci. 97 (2018) 22–34.
[5] A. Azarniya, A.K. Taheri, K.K. Taheri, Recent advances in ageing of 7xxx series aluminum alloys: a physical metallurgy perspective, J. Alloys Compd. 781 (2019) 945–983.
[6] G. Çam, G. İpekoğlu, Recent developments in joining of aluminum alloys, Int. J. Adv. Manuf. Technol. 91 (2017) 1851–1866.
[7] C. Zhang, G. Huang, Y. Cao, Y. Zhu, Q. Liu, On the microstructure and mechanical properties of similar and dissimilar AA7075 and AA2024 friction stir welding joints: effect of rotational speed, J. Manuf. Process. 37 (2019) 470–487.
[8] P. Threadgill, A. Leonard, H. Shercliff, P. Withers, Friction stir welding of aluminium alloys, Int. Mater. Rev. 54 (2009) 49–93.
[9] G. Çam, Friction stir welded structural materials: beyond Al-alloys, Int. Mater. Rev. 56 (2011) 1–48.
[10] C. Zhang, Y. Cao, G. Huang, Q. Zeng, Y. Zhu, X. Huang, et al., Influence of tool rotational speed on local microstructure, mechanical and corrosion behavior of dissimilar AA2024/7075 joints fabricated by friction stir welding, J. Manuf. Process. 49 (2020) 214–226.
[11] W. Thomas, E. Nicholas, J.C. Needham, M. Murch, P. Templesmith, C. Dawes, Friction Stir Welding, International Patent Application No. PCT/GB92102203 and Great Britain Patent Application, (1991).
[12] A. Bayazid, M. Heddad, I. Cayiroglu, A review on friction stir welding, parameters, microstructure, mechanical properties, post weld heat treatment and defects, Mater. Sci. Eng. 2 (2018) 116–126.
[13] R.S. Mishra, Z. Ma, Friction stir welding and processing, Mater. Sci. Eng. R 50 (2005) 1–78.
[14] R. Nandan, T. DebRoy, H. Bhadeshia, Recent advances in friction-stir welding–-process, weldment structure and properties, Prog. Mater. Sci. 53 (2008) 980–1023.
[15] R.A. Gite, P.K. Loharkar, R. Shimpi, Friction stir welding parameters and application: a review, Mater. Today: Proc. 19 (2019) 361–365.
[16] C. Zhang, G. Huang, Y. Cao, Y. Zhu, W. Li, X. Wang, et al., Microstructure and mechanical properties of dissimilar friction stir welded AA2024-7075 joints: influence of joining material direction, Mater. Sci. Eng. A 766 (2019) 138368.
[17] S. Rajakumar, C. Muralidharan, V. Balasubramanian, Influence of friction stir welding process and tool parameters on strength properties of AA7075-T6 aluminium alloy joints, Mater. Des. 32 (2011) 535–549.
[18] S. Rajakumar, C. Muralidharan, V. Balasubramanian, Optimization of the friction-stir-welding process and tool parameters to attain a maximum tensile strength of AA7075–T6 aluminium alloy, P. I. Mech. Eng. B-J. Eng. 224 (2010) 1175–1191.
[19] K.K. Mugada, K. Adepu, Role of scroll shoulder and pin designs on axial force, material flow and mechanical properties of friction stir welded Al–Mg–Si alloy, Met. Mater. Int. (2020) 1–12.
[20] K.K. Mugada, K. Adepu, Influence of ridges shoulder with polygonal pins on material flow and friction stir weld characteristics of 6082 aluminum alloy, J. Manuf. Process. 32 (2018) 625–634.
[21] L. Shi, C. Wu, L. Fu, Effects of tool shoulder size on the thermal process and material flow behaviors in ultrasonic vibration enhanced friction stir welding, J. Manuf. Process. 53 (2020) 69–83.
[22] V. Saravanan, S. Rajakumar, N. Banerjee, R. Amuthakkannan, Effect of shoulder diameter to pin diameter ratio on microstructure and mechanical properties of dissimilar friction stir welded AA2024-T6 and AA7075-T6 aluminum alloy joints, Int. J. Adv. Manuf. Technol. 87 (2016) 3637–3645.
[23] Y. Mao, L. Ke, F. Liu, Q. Liu, C. Huang, L. Xing, Effect of tool pin eccentricity on microstructure and mechanical properties in friction stir welded 7075 aluminum alloy thick plate, Mater. Des. 62 (2014) 334–343.
[24] A. Arora, A. De, T. DebRoy, Toward optimum friction stir welding tool shoulder diameter, Scr. Mater. 64 (2011) 9–12.
[25] G. Chen, S. Zhang, Y. Zhu, C. Yang, Q. Shi, Thermo-mechanical analysis of friction stir welding: a review on recent advances, Acta Metall. Sin. (Engl. Lett.) 33 (2020) 3–12.
[26] S.K. Hussein, Theoretical analysis, finite element method and optimization of heat generation in friction stir welding from different probe and shoulder profiles, Int. J. Adv. Res. 4 (2016).
[27] S. Rajakumar, C. Muralidharan, V. Balasubramanian, Developing empirical relationships to predict grain size and hardness of the weld nugget of friction stir welded AA7075-T 6 aluminium alloy joints, Exp. Tech. 36 (2012) 6–17.
[28] R. Leal, C. Leitao, A. Loureiro, D. Rodrigues, P. Vilaça, Material flow in heterogeneous friction stir welding of thin aluminium sheets: effect of shoulder geometry, Mater. Sci. Eng. A 498 (2008) 384–391.
[29] K.K. Mugada, K. Adepu, Role of tool shoulder end features on friction stir weld characteristics of 6082 aluminum alloy, J. Inst. Eng. India Ser. C 100 (2019) 343–350.
[30] K.K. Mugada, K. Adepu, Influence of tool shoulder end features on friction stir weld characteristics of Al-Mg-Si alloy, Int. J. Adv. Manuf. Technol. 99 (2018) 1553–1566.
[31] L. Trueba Jr., G. Heredia, D. Rybicki, L.B. Johannes, Effect of tool shoulder features on defects and tensile properties of friction stir welded aluminum 6061-T6, J. Mater. Process. Technol. 219 (2015) 271–277.
[32] Y.K. Periyasamy, A.V. Perumal, B.K. Periyasamy, Influence of tool shoulder concave angle and pin profile on mechanical properties and microstructural behaviour of friction stir welded AA7075-T651 and AA6061 dissimilar joint, Trans. Indian Inst. Met. 72 (2019) 1087–1109.
[33] R. Padmanaban, V. Balusamy, R. Vaira Vignesh, Effect of friction stir welding process parameters on the tensile strength of dissimilar aluminum alloy AA2024-T3 and AA7075-T6 joints, Materialwiss. Werkst. 51 (2020) 17–27.
[34] Z. Zhang, Y. Liu, J. Chen, Effect of shoulder size on the temperature rise and the material deformation in friction stir welding, Int. J. Adv. Manuf. Technol. 45 (2009) 889.
[35] S.R. Nathan, V. Balasubramanian, S. Malarvizhi, A. Rao, Effect of tool shoulder diameter on stir zone characteristics of friction stir welded HSLA steel joints, Trans. Indian Inst. Met. 69 (2016) 1861–1869.
[36] M. Vignesh Kumar, G. Padmanaban, V. Balasubramanian, Role of tool pin profiles on wear characteristics of friction stir processed magnesium alloy ZK60/silicon carbide surface composites, Materialwiss. Werkst. 51 (2020) 140–152.
[37] M. Raturi, A. Garg, A. Bhattacharya, Joint strength and failure studies of dissimilar AA6061-AA7075 friction stir welds: effects of tool pin, process parameters and preheating, Eng. Failure Anal. 96 (2019) 570–588.
[38] P. Prakash, R.S. Anand, S.K. Jha, Prediction of weld zone shape with effect of tool pin profile in friction stir welding process, J. Mech. Sci. Technol. 34 (2020) 279–287.
[39] R. Venkateswara Rao, M. Senthil Kumar, Effect of pin geometry on material flow characteristics of friction stir welded dissimilar AA6061/AA2014 alloys, Aust. J. Mech. Eng. (2020) 1–15.
[40] Z. Sun, C. Wu, Influence of tool thread pitch on material flow and thermal process in

friction stir welding, J. Mater. Process. Technol. 275 (2020) 116281.
[41] M. Ahmed, B. Wynne, W. Rainforth, A. Addison, J. Martin, P. Threadgill, Effect of tool geometry and heat input on the hardness, grain structure, and crystallographic texture of thick-section friction stir-welded aluminium, Metall. Mater. Trans. A 50 (2019) 271–284.
[42] C. Zhang, G. Huang, Y. Cao, X. Wu, X. Huang, Q. Liu, Optimization of tensile and corrosion properties of dissimilar friction stir welded AA2024-7075 joints, J. Mater. Eng. Perform. 28 (2019) 183–199.
[43] Z. Chenghang, H. Guangjie, C. Yu, L. Wei, L. Qing, EBSD analysis of nugget zone in dissimilar friction stir welded AA2024-AA7075 joint along weld thickness, Rare Metal Mater. Eng. 48 (2019) 3161–3166.
[44] J. Przydatek, A ship classification view on friction stir welding, First International Symposium on Friction Stir Welding, Thousand Oaks, CA. Cambridge, UK: The Welding Institute Ltd, 1999.
[45] A. Scialpi, L. De Filippis, P. Cavaliere, Influence of shoulder geometry on microstructure and mechanical properties of friction stir welded 6082 aluminium alloy, Mater. Des. 28 (2007) 1124–1129.
[46] G. Cam, S. Mistikoglu, Recent developments in friction stir welding of Al-alloys, J. Mater. Eng. Perform. 23 (2014) 1936–1953.
[47] M. Ghosh, K. Kumar, R. Mishra, Analysis of microstructural evolution during friction stir welding of ultrahigh-strength steel, Scr. Mater. 63 (2010) 851–854.
[48] F. Liu, L. Fu, H. Chen, Effect of high rotational speed on temperature distribution, microstructure evolution, and mechanical properties of friction stir welded 6061-T6 thin plate joints, Int. J. Adv. Manuf. Technol. 96 (2018) 1823–1833.
[49] K.A. Hassan, P. Prangnell, A. Norman, D. Price, S. Williams, Effect of welding parameters on nugget zone microstructure and properties in high strength aluminium alloy friction stir welds, Sci. Technol. Weld. Join. 8 (2003) 257–268.
[50] A. Gholinia, F. Humphreys, P. Prangnell, Production of ultra-fine grain microstructures in Al–Mg alloys by coventional rolling, Acta Mater. 50 (2002) 4461–4476.
[51] Z. Ma, A. Feng, D. Chen, J. Shen, Recent advances in friction stir welding/processing of aluminum alloys: microstructural evolution and mechanical properties, Crit. Rev. Solid State 43 (2018) 269–333.
[52] M. Imam, V. Racherla, K. Biswas, H. Fujii, V. Chintapenta, Y. Sun, et al., Microstructure-property relation and evolution in friction stir welding of naturally aged 6063 aluminium alloy, Int. J. Adv. Manuf. Technol. 91 (2017) 1753–1769.
[53] D.P. Field, T.W. Nelson, Y. Hovanski, K.V. Jata, Heterogeneity of crystallographic texture in friction stir welds of aluminum, Metall. Mater. Trans. A 32 (2001) 2869–2877.
[54] M.M. Moradi, H.J. Aval, R. Jamaati, S. Amirkhanlou, S. Ji, Effect of SiC nanoparticles on the microstructure and texture of friction stir welded AA2024/AA6061, Mater. Charact. 152 (2019) 169–179.
[55] F.J. Humphreys, M. Hatherly, Recrystallization and Related Annealing Phenomena, Elsevier, 2012.
[56] M.M. Moradi, H.J. Aval, R. Jamaati, S. Amirkhanlou, S. Ji, Microstructure and texture evolution of friction stir welded dissimilar aluminum alloys: AA2024 and AA6061, J. Manuf. Process. 32 (2018) 1–10.
[57] N. Nadammal, S.V. Kailas, J. Szpunar, S. Suwas, Development of microstructure and texture during single and multiple pass friction stir processing of a strain hard-enable aluminium alloy, Mater. Charact. 140 (2018) 134–146.
[58] C. He, Y. Li, Z. Zhang, J. Wei, X. Zhao, Investigation on microstructural evolution and property variation along building direction in friction stir additive manufactured Al–Zn–Mg alloy, Mater. Sci. Eng. A (2020) 139035.
[59] Y. Min, R.-j. Bao, X.-z. Liu, C.-q. Song, Thermo-mechanical interaction between aluminum alloy and tools with different profiles during friction stir welding, Trans. Nonferrous Met. Soc. 29 (2019) 495–506.
[60] F. Liu, Z. Sun, Y. Tuo, Y. Ji, Y. Bai, Effect of shoulder geometry and clamping on microstructure evolution and mechanical properties of ultra-thin friction stir-welded Al6061-T6 plates, Int. J. Adv. Manuf. Technol. 106 (2020) 1465–1476.
[61] R. Fonda, J. Bingert, Texture variations in an aluminum friction stir weld, Scr. Mater. 57 (2007) 1052–1055.
[62] J. Shen, F. Wang, U.F. Suhuddin, S. Hu, W. Li, J.F. Dos Santos, Crystallographic texture in bobbin tool friction-stir-welded aluminum, Metall. Mater. Trans. A 46 (2015) 2809–2813.
[63] M. Yuqing, K. Liming, L. Fencheng, C. Yuhua, X. Li, Investigations on temperature distribution, microstructure evolution, and property variations along thickness in friction stir welded joints for thick AA7075-T6 plates, Int. J. Adv. Manuf. Technol. 86 (2016) 141–154.
[64] M.M. Hasan, M. Ishak, M. Rejab, Effect of pin tool flute radius on the material flow and tensile properties of dissimilar friction stir welded aluminum alloys, Int. J. Adv. Manuf. Technol. 98 (2018) 2747–2758.
[65] C. Zhang, G. Huang, Y. Cao, Y. Zhu, X. Huang, Y. Zhou, et al., Microstructure evolution of thermo-mechanically affected zone in dissimilar AA2024/7075 joint produced by friction stir welding, Vacuum (2020) 109515.
[66] X. Zhu, P. Blake, K. Dou, S. Ji, Strengthening die-cast Al-Mg and Al-Mg-Mn alloys with Fe as a beneficial element, Mater. Sci. Eng. A 732 (2018) 240–250.